Integrative transcriptomic analysis of tissue-specific metabolic crosstalk after myocardial infarction

Muhammad Arif[1, #], Martina Klevstig[2, #], Rui Benfeitas[3], Stephen Doran[4], Hasan Turkez[5], Mathias Uhlén[1], Maryam Clausen[6], Johannes Wikström[7], Damla Etal[6], Cheng Zhang[1], Malin Levin[2], Adil Mardinoglu[1, 4, *], Jan Boren[2, *]

[1]Science for Life Laboratory, KTH - Royal Institute of Technology, Stockholm, SE-17121, Sweden.

[2]Department of Molecular and Clinical Medicine, University of Gothenburg, The Wallenberg Laboratory, Sahlgrenska University Hospital, Gothenburg, Sweden.

[3]National Bioinformatics Infrastructure Sweden (NBIS), Science for Life Laboratory, Department of Biochemistry and Biophysics, Stockholm University, S-10691 Stockholm, Sweden

[4]Centre for Host-Microbiome Interactions, Faculty of Dentistry, Oral & Craniofacial Sciences, King's College London, London, SE1 9RT, United Kingdom.

[5]Department of Medical Biology, Faculty of Medicine, Atatürk University, Erzurum, 25240, Turkey.

[6]Translational Genomics, BioPharmaceuticals R&D, Discovery Sciences, AstraZeneca, Gothenburg, Sweden.

[7]Bioscience Cardiovascular, Research and Early Development, Cardiovascular, Renal and Metabolism (CVRM), BioPharmaceuticals R&D, AstraZeneca, Gothenburg, Sweden

[#]Contributed equally.

*Corresponding authors: Adil Mardinoglu and Jan Boren

Email: adilm@scilifelab.se; Jan.Boren@wlab.gu.se

Abstract/Summary

Myocardial infarction (MI) promotes a range of systemic effects, many of which are unknown. Here, we investigated the alterations associated with MI progression in heart and other metabolically active tissues (liver, skeletal muscle, and adipose) in a mouse model of MI (induced by ligating the left ascending coronary artery) and sham-operated mice. We performed a genome-wide transcriptomic analysis on tissue samples obtained 6- and 24-hours post MI or sham operation. By generating tissue-specific biological networks, we observed: (1) dysregulation in multiple biological processes (including immune system, mitochondrial dysfunction, fatty-acid beta-oxidation, and RNA and protein processing) across multiple tissues post MI; and (2) tissue-specific dysregulation in biological processes in liver and heart post MI. Finally, we validated our findings in two independent MI cohorts. Overall, our integrative analysis highlighted both common and specific biological responses to MI across a range of metabolically active tissues.

Keywords

Systems biology; network analysis; whole-body modelling; cardiovascular disease; Myocardial infarction; multi-tissue; metabolically active tissues; liver; adipose; muscle

Introduction

Cardiovascular disease (CVD) is the leading cause of death worldwide, accounting for more than 17 million deaths globally in 2016 [1]. Myocardial infarction (MI) is one of the most common causes of CVD-related death, and is the result of severe coronary artery disease that develops from tapered arteries or chronic blockage of the arteries caused by accumulation of cholesterol or plaque (atherosclerosis). MI has been linked to multiple behavioral risk factors (including unhealthy diet, physical inactivity, excessive use of alcohol, and tobacco consumption) that can lead to significant alterations in metabolism that are responsible for hypertension, obesity, diabetes, and hyperlipidemia. These abnormalities are known as the high-risk factors of MI and CVDs in general.

Systems biology has been used in many studies to reveal the underlying molecular mechanisms of complex human diseases and to answer important biological questions related to the progression, diagnosis and treatment of the diseases. The use of systems biology has aided the discovery of new therapeutic approaches in multiple diseases [2-4] by identifying novel therapeutic agents and repositioning of existing drugs [5]. Systems biology has also been employed in the identification of novel biomarkers, characterization of patients and stratification of heterogenous cancer patients [6-8]. Specifically, integrated networks (INs) [8] and co-expression networks (CNs) [9] have been proven to be robust methods for revealing the key driver of metabolic abnormalities, discovering new therapy strategies, as well as gaining systematic understanding of diseases [10,11].

Previously, multiple studies in individual tissues have been performed and provided new insights into the underlying mechanisms of diseases [12-15]. However, the crosstalk between different tissues and their dysregulation has not been examined in MI and other CVD-related complications [16]. Here we performed an integrated analysis of heart and other metabolically active tissues (liver, skeletal muscle and adipose tissue) using a mouse model of MI. We used several systems biology approaches to obtain a systematic picture of the metabolic alterations that occur after an MI (**Figure 1A**), and validated our findings in two independent datasets.

Results

Differential expression analysis shows a pronounced effect on gene expression 24 h post MI

To study global biological alterations and systemic whole-body effects associated with MI, we obtained heart, liver, skeletal muscle, and white adipose tissue from mice 6 h and 24 h after either an MI (induced by ligating the left ascending coronary artery) or a sham operation (as control). We generated transcriptomics data and identified differentially expressed genes (DEGs) 6 and 24 h post MI and sham operation in all tissues, with the most significant differences occurring after 24 h **(Table S1, Figure 1B)**. Principal component analysis (PCA) showed a close clustering between the control (for both time points) and MI (6 h and 24 h separately) samples for heart tissue but clustering by extraction time points (6 h and 24 h clusters) for the other tissues (**Figure S1**). We present the transcriptional changes associated with MI in **Table S1** and the DEGs (FDR < 5%) using an UpSet plot [17] in **Figure 1C**.

All tissues showed a more pronounced effect in terms of the number of DEGs 24 h post MI (**Figure 1C**). As expected, the most affected tissue was the heart (393 DEGs at 6 h, 3318 DEGs at 24 h, and 318 DEGs were the same at both time points). By contrast, 136, 641 and 374 genes were significantly changed in liver, skeletal muscle and adipose tissues 24 h post MI compared to control, respectively. More than 33% of the DEGs that significantly changed in the other tissues also changed in the heart (**Figure 1C**). Interestingly, more than 97% of the shared DEGs between heart and skeletal muscle changed in the same direction, with corresponding numbers of 88% and 64% in adipose and liver, respectively.

Functional analysis reveals widespread mitochondrial, fatty acid, immune, and protein and RNA-related alterations post MI with liver shows contrasting trend

We performed gene-set enrichment analysis (GSEA) with KEGG pathways (**Table S2, Figure 1D**) and gene ontology (GO) biological processes (BPs) (**Table S3, Figure 2A**) to identify altered biological functions and pathways 24 h after an MI. Mitochondrial functions (specifically, mitochondrial translation, respiratory chain and oxidative phosphorylation) were significantly downregulated in the heart, muscle and adipose tissues but not in the liver. Processes related to oxidative stress were upregulated in the heart and skeletal muscle. Fatty acid beta-oxidation was downregulated in the heart and adipose but upregulated in the liver. Processes and pathways related to immune systems were significantly upregulated in the heart

and skeletal muscle but significantly downregulated in liver. Processes associated with protein and RNA processing, ribosome biogenesis and protein targeting endoplasmic reticulum were upregulated in all tissues except liver whereas protein processing in endoplasmic reticulum and RNA transport pathways were upregulated in all tissues.

We also observed that liver was showing opposite trends compared to the other tissues in other important functions, such as fatty acid metabolism and immune response. By checking regulation at the gene level, we observed that only 16 DEGs in liver showed opposite regulation compared to the other tissues whereas 97 out of the 136 DEGs in liver were not DEGs in any other tissues (**Table S4**). Therefore, the differences we observed in liver were mainly due to different DEGs rather than opposite regulation compared to other tissues.

Tissue-specific altered biological functions point to specificity of metabolic and signaling responses to MI

The functional analysis also indicated that several metabolic pathways (including cholesterol, ascorbate and aldarate, linoleic acid, and sphingolipid metabolism pathways) and signaling pathways (including GnRH, FoxO, cAMP and prolactin signaling pathways) were significantly upregulated in heart 6 h after an MI (**Table S2**, **Figure S2A**). We also observed significant down regulation of tryptophan metabolism and upregulation of glycosaminoglycan biosynthesis in heart 24 h after an MI (**Table S2**, **Figure S2A**). Processes related to retinol metabolism were upregulated in heart at both timepoints. Pathways that were previously associated with cardiac hypertrophy and cardiac remodeling (e.g. JAK-STAT, MAPK, estrogen, and TNF signaling pathways, and ECM-receptor interaction) were significantly upregulated in heart 6 and 24 h after an MI (**Figure S1B**).

Our analysis also indicated significant metabolic differences in adipose tissue 24 h after an MI (**Figure S2B**). Fructose and mannose metabolism, glyoxylate and dicarboxylate metabolism, glycolysis/gluconeogenesis, and pentose phosphate pathways, glycine, serine and threonine metabolism and pyrimidine metabolism, as well as endocrine systems (e.g. insulin signaling pathway and regulation of lipolysis in adipocytes) were downregulated in adipose tissue. We observed that the PPAR signaling pathway was upregulated whereas glutathione was downregulated in liver 24 h post-infarction (**Figure S2B**). We found that sphingolipid metabolism and immune-related pathways were upregulated in skeletal muscle 24 h post-infarction (**Figure S2B**).

146

147 ***Reporter metabolite analyses show significant alterations in fatty acid, amino acid, retinol,***
148 ***and estrogen metabolism post MI***

149 To predict the effect of the transcriptional changes on metabolism, we performed reporter
150 metabolite analyses (**Table S5**) using the gene-to-metabolites mapping from the Mouse
151 Metabolic Reaction database [18]; results in each tissue 24 h after MI are shown in **Figure 2B**.
152 In agreement with our analyses above, reporter metabolites related to oxidative
153 phosphorylation, such as *ubiquinol*, *ubiquinone*, *NADH* and *NAD+*, were downregulated in all
154 tissues except liver. Moreover, *linolenoyl-CoA, acetyl CoA,* and several other fatty acyl-CoA-
155 related metabolites were downregulated in heart and adipose tissue but upregulated in liver.
156 We also found that several *5-S-glutathionyl* metabolite forms, known to be related to
157 phenylalanine, tyrosine and tryptophan biosynthesis, were downregulated in heart, liver and
158 skeletal muscle. The same pattern of downregulation was also observed for metabolites
159 related to estrogen metabolism, specifically metabolites related to oestrone and its glutathione
160 conjugate derivative. Moreover, *12-keto-LTB4* and *12-oxo-c-LTB3*, related to leukotriene
161 metabolism, and *hepoxilin A3,* an arachidonic acid, were also found to be downregulated in
162 heart, liver, and skeletal muscle.

163

164 The liver showed the highest alteration in reporter metabolites, which is attributed to its role
165 as one of the most metabolically active tissues. We found that several reporter metabolites
166 related to retinol metabolism, namely *retinal*, *retinol*, *retinoate*, and *all-trans-18-*
167 *hydroxyretinoic acid*, were significantly downregulated only in liver tissue. Retinol
168 metabolism has been previously associated with MI [19,20].

169

170 ***Network analyses unveil universal and tissue-specific clusters and mechanisms post MI***

171 The use of co-expression network (CN) analyses can assist in elucidating the functional
172 relationships between genes in a specific cell and tissue [9]. Here, we performed CN analysis to
173 reveal the functional relationship between the DEGs by generating tissue-specific CNs and
174 selected highly connected genes (the top 5% positively correlated genes that fulfilled FDR <
175 0.05) (**Table 1**). To better define the structure of the networks, we used the Leiden clustering
176 algorithm [21] by maximizing the modularity scores (**Figure 3A-D**) and selected the clusters
177 that include more than 30 genes. Next, we superimposed DEGs 24 h post-infarction onto the
178 network (**Table S1**) and identified the components of the clusters that were affected by an MI.

We also used functional analysis with GO BP and KEGG pathways to understand the specific functions associated with each cluster by using the Enrichr algorithm (FDR < 0.05) [22,23]. We summarized the GO BP terms with Revigo (**Table S6**) [24] and checked the average clustering coefficient to define the centrality of each cluster (**Table S6**) [9]. Among the clusters, we identified the key clusters as those with the highest average clustering coefficient, allowing us to identify sets of genes whose time-dependent coordinated changes showed the strongest relationships.

Interestingly, key clusters contained genes with similar functionalities including RNA processing, transports, and RNA metabolic processes in all tissue-specific CNs (**Table S6**). In addition, we found that the majority of the DEGs associated with those clusters were significantly upregulated. These observations strengthen the findings of the functional analysis above (**Figure 2A**) and further highlight how embryonically distinct tissues display similar functional responses to MI, with the most highly connected groups of genes preserved between different tissues (**Table S6**, **Figure 3E**).

Community detection reveals tissue-specific clusters post MI

We investigated the tissue specificity of each cluster by performing enrichment analysis with data from the Mouse Gene Atlas [25], which involved counting the number of tissue-specific genes.

The heart network showed the highest number of tissue-specific genes in cluster Heart-3 (302 genes). Based on DEG analysis, we found that 522 genes were downregulated and 192 genes were upregulated in the cluster. The enriched GO BP terms in the cluster were mitochondrial transport, protein processing and respiratory chain, cardiac muscle cell action potential, response to muscle stretch, and heart contraction (**Figure 3F**). We observed that the results of the KEGG pathway enrichment analysis were consistent with those obtained from GO BP analysis (**Table S6**).

In the liver network, cluster Liver-2 showed the highest tissue specificity (479 genes). In this cluster, we found that 15 genes were significantly downregulated and 17 genes were significantly upregulated. Based on GO BP enrichment analysis, the genes in this cluster were associated with cholesterol metabolism and homeostasis, lipid transport, glutathione

metabolism, lipoprotein metabolism, and glucose 6-phosphate metabolism (**Table S6**). KEGG enrichment analysis also showed that the genes in the cluster were related to retinol, carbohydrate, lipid and amino-acid metabolism (**Table S6**).

The muscle network had two clusters with high tissue specificity: cluster Muscle-4 (276 genes) and Muscle-5 (143 genes). Muscle-4 showed association with GO BP terms such as mitochondrial transport, protein processing and respiratory chain, response to muscle stretch, and muscle contraction (**Table S6**). In contrast, the KEGG pathway in this cluster showed relation to glycolysis/glucogenesis, propanoate metabolism, glyoxylate and dicarboxylate metabolism, and several signaling pathways (e.g. oxytocin, glucagon, cGMP-PKG and HIF-1) (**Table S6**). Muscle-5 was enriched in GO BP terms associated with protein dephosphorylation, muscle contraction and intracellular protein transport (**Table S6**). We also found that insulin, MAPK and Wnt signaling pathways were associated to Muscle-5 from the KEGG enrichment analysis (**Table S6**).

The adipose tissue network showed tissue specificity in cluster Adipose-2 (33 genes), which is associated with GO BP processes including mRNA processing, regulation of mitotic cell cycle phase, ribosome biogenesis, and viral processes (**Table S6**). We observed that the results of the KEGG pathway enrichment analysis were consistent with those obtained from GO BP analysis, with additional associations with multiple signaling and regulatory pathways (**Table S6**).

Tissue-specific clusters show important tissue-specific changes post MI

To understand the specific behavior of each tissue, we further studied the tissue-specific clusters in the CNs (**Figure 4A**). Heart specific cluster, Heart-3, was driven by several central genes including *Pln*, *Pde4b*, and *Atp2a2* (related to regulation of cardiac muscle contraction) and Pdha*1* and *Vdac1* (related to mitochondrial functions). These genes were also found to be significantly differentially expressed in heart 24 hours post MI (**Table S1**). Genes in the heart-specific cluster were related to multiple other processes/pathways, e.g. oxytocin signaling pathway, and several metabolic pathways (glycogen, inositol phosphate and purine) (**Table S6**).

Mitochondrial dysfunction in the heart leads to disturbance of energy (ATP) production [26,27] and, in the presence of oxygen, to accumulation of reactive oxygen species (ROS), which can cause oxidative stress. *Vdac1*, a key gene for regulation of mitochondria function and one of the central genes in the heart-specific cluster (see above), is significantly downregulated in MI [28]. *Vdac1* is located in the outer mitochondrial membrane and is involved directly in cardioprotection [29] within the cGMP/PKG pathway (**Figure S3A**). In the same pathway, we also observed down-regulation of the reporter metabolite hydrogen peroxide (**Table S5**), a ROS that is related to cardioprotection [29,30]. We also observed downregulation of *Pdha1*, which is known to have a substantial role in both the HIF-1 signaling pathway and the pyruvate metabolism pathway that converts pyruvate to acetyl-CoA in the mitochondria (**Figure S3B**). Acetyl-CoA is used in the TCA cycle to produce NADH and FADH2, which are both needed for ATP production and were downregulated in our reporter metabolite analysis of the heart. Our findings are thus consistent with dysfunctional mitochondria and ATP production in the heart in response to an MI. *Pdha1* has been also been linked to the heart sensitivity during to ischemic stress, where its deficiency can compromise AMP-activated protein kinase activation [31].

In skeletal muscle and adipose tissue, we found that central genes in their respective tissue-specific clusters related to fatty acid metabolism and lipid metabolism were significantly altered (**Table S6**, **Figure 5**). In liver-specific cluster, we found that their central genes were related to fatty-acid beta oxidation (*Cyp4a31*, *Cyp4a32*) and glutathione metabolism (*Gstm3*) (**Table S6**, **Figure 5A**). Alterations of fatty acid beta-oxidation and glutathione metabolism have previously been reported in non-alcoholic fatty liver disease, a known risk factor of CVD [32,33]. Moreover, in liver, we also found that retinol metabolism was uniquely related to genes in the liver-specific cluster, mainly driven by four significantly differentially expressed central genes of the clusters, i.e. *Cyp26a1*, *Cyp4a31*, *Cyp4a32*, and *Hsd17b6* (**Table S6**). A previous study showed that mortality from CVD in older individuals was accompanied by impaired liver ability to store retinol [19].

Multi-tissue modeling reveals key metabolic pathways affected post MI

To investigate the metabolic responses to MI in and across tissues in the mice, we constructed a multi-tissue genome-scale metabolic model. The model consisted of five tissue-specific genome scale metabolic models, namely heart, liver, skeletal muscle, adipose, and small

intestine. The small intestine model (for which we do not have transcriptomic data) was added to include ingestion and conversion of dietary nutrients into chylomicrons, which are directly secreted into blood and transport lipids to other tissues [18]. The final mouse multi-tissue model included 19,859 reactions, 13,284 metabolites, 7,116 genes and 41 compartments. We predicted the metabolic fluxes in mice 24 h after an MI or sham operation by integrating the dietary input, tissue-specific resting energy expenditure and transcriptomics data.

The modeling showed that oxygen uptake, carbon dioxide production and the oxidative phosphorylation pathway in heart, adipose and skeletal muscle were decreased in MI mice, in agreement with the downregulation of oxidative phosphorylation we observed in these tissues (**Table S7**). By contrast, liver showed slightly increased oxygen uptake, which might due to the slightly (not statistically significant) upregulated oxidative phosphorylation (**Table S7**). These findings indicate that the changes in oxygen and carbon dioxide fluxes and the oxidative phosphorylation pathway could serve as a positive control for predicting the changes due to MI in the fluxes.

Next, we investigated the tissue-specific metabolic flux changes in the same model (**Table S7**). We found that the pentose phosphate pathway was upregulated in heart 24 hours post MI, consistent with upregulated glucose metabolism after an MI. Elevated glycolysis could allow the heart to rapidly generate energy under stress conditions, and the enhanced pentose phosphate pathway could increase the NADPH level, which could help maintain the level of reduced glutathione in heart [34]. We also found that adipose tissue secreted more ketone bodies, including acetoacetate and butyrate, into plasma; the plasma level of ketone bodies has been reported as a stress marker in acute MI [35]. Notably, relatively small metabolic changes were found in liver and skeletal muscle, which is probably due to the small number of transcriptomic changes in metabolic pathways in these tissues.

Validating our findings with publicly available datasets

We validated our observations in heart tissue in two independent cohorts of bulk RNA-seq data from mouse heart (**Table S8**). We filtered both validation cohorts to get and analyzed only 24 hours post-MI data. We found that there were 2169 DEGs in heart 24 h after infarction from our data were validated in at least one of the independent cohorts (959 in both) (**Figure 6A)**. We also found that 109 out of the 123 most connected genes in our heart-

specific cluster were also significantly differentially expressed in at least one of the independent cohorts (81 in both). By performing functional analysis of the validation cohorts, we found that ~61% of GO BP and 84% of KEGG pathways identified in our analysis of the heart were also present in at least one of the validation cohorts 24 h after infarction (**Figure 6B-C**). In both cohorts, we observed downregulation of mitochondrial functions and fatty acid metabolism processes. We also observed upregulation of processes and pathways related to retinol metabolism and inflammatory response in both validation cohorts.

Identification of driver genes in MI

We observed that *Flnc*, *Lgals3*, *Prkaca* and *Pprc1* showed important response to MI. These genes were 4 of 16 genes that were DEGs in at least three tissues and validated in both validation cohorts (**Table S9**). *Flnc*, *Lgals3* and *Pprc1* were upregulated in heart, skeletal muscle, and adipose, whereas *Prkaca* was downregulated in these three tissues. We further retrieved their neighbors at each tissue specific CNs, showed their regulations from differential expression results, and performed functional analysis in **Table S9**.

Flnc, which encodes filamin-C, was part of heart and skeletal muscle-specific CN cluster (**Figure S4**). Its neighbor genes were found to be significantly (FDR < 0.05) associated to several functions, including TCA cycle, pyruvate metabolism, glycolysis pathway, and involved in mitochondrial functions. Specifically, they were related to heart-specific processes in heart, VEGF signaling pathway in muscle, carbohydrate metabolism in adipose, and to MAPK signaling pathway and muscle contraction in heart and muscle.

Lgals3 (encodes galectin-3) and *Prkaca* were among the most central genes in central clusters (**Table S6**). The neighbors of *Lgals3* were significantly related to cell cycle and protein digestion and absorption pathway in all tissues, and to RNA and mRNA related-processes in muscle and adipose tissue. The neighbors of *Prkaca* were related to insulin signaling pathway in heart and adipose, and several mitochondrial functions in adipose. *Pprc1* was part of most central clusters in heart and adipose tissue CN, and its neighbors were related to ribosomal RNA processing and ribosome biogenesis.

Discussion

CVD has a complex etiology and is responsible for a range of systemic effects, hindering our understanding of its consequences on different tissues. Here, we took advantage of the technological advances in high-throughput RNA-seq and applied integrative network analyses to comprehensively explore the underlying biological effects of MI. Specifically, we generated RNA-seq data from heart, liver, skeletal muscle and adipose tissue obtained from mice 6 and 24 h after an MI or sham operation. We used transcriptomics data analyses (differential expression, functional analysis, and reporter metabolites analysis) to determine the systemic effects of the MI across multiple tissues. Moreover, we performed CN analyses to pinpoint important key and tissue-specific clusters in each tissue, and identified the key genes in each cluster. Finally, we used a whole-body modelling approach to identify the crosstalk between tissues and reveal the global metabolic alterations, before finally validating our findings with publicly available independent MI cohorts.

Based on our analyses, we observed downregulation of heart-specific functions and upregulation of lipid metabolism and inflammatory response in heart, muscle, and adipose tissue after an MI (**Figure 4B**). Liver showed a distinct response with respect to the other three tissues, including downregulation of inflammatory response. We observed that fatty acid metabolism was downregulated in heart and adipose tissue, whereas fatty acid beta-oxidation was upregulated and glutathione metabolism was downregulated in liver. We also observed upregulation of oxidative stress in heart and skeletal muscle. We also observed downregulation of mitochondrial functions in heart, muscle, and adipose tissue. Furthermore, we found upregulation of retinol metabolism in heart and downregulation of retinol metabolites in liver (**Figure 4B**).

We hypothesized that downregulation of fatty acid metabolism from adipose tissue was due to exchange of fatty acids with other tissues (liver and muscle) (**Figure 4B**). We also observed the flow of retinol from liver to heart during MI, consistent with previous reports [20]. These MI-associated alterations lead to dysfunctional mitochondria and decreased energy production, especially in heart and skeletal muscle.

We also validated our results with publicly available MI datasets generated in separate independent studies. The validation results strengthened our findings on the altered functions/pathways and the important heart-specific genes after an MI.

Importantly, our analyses of gene clusters highlighted multiple key genes in the response to MI in different tissues. Specifically, we observed that *Flnc*, *Prkaca, Lgals3*, and *Pprc1* showed important responses in heart, skeletal muscle, and adipose tissue. *Flnc* is involved in actin cytoskeleton organization in heart and skeletal muscle, and previous studies have shown that this gene has critical role in CVD [36,37]. Similarly, *Prkaca,* an important metabolic gene, has also been shown to play an important function during CVD [38-40]. *Lgals3*, related to acute inflammation response, has been studied intensively in recent years as a key gene in CVD, and as a potential CVD therapy target [41,42]. Lastly, *Pprc1*, as important regulator of mitochondrial biogenesis, has not been explored for its direct relationship with CVD; however, mitochondrial biogenesis appears to be an important response to CVD [43-45].

We recognized several limitations to be noted on this research. First, only transcriptomic data was analyzed in this research, hence the sensitivity might be limited especially for short timepoint, e.g. 6 hours after MI. Second, we focused our analysis in this research only on protein-coding genes. Third, to explore more about the shift in metabolism due to MI, longer timepoints needs to be explored. This opens new opportunities for future research, including analyzing the non-protein-coding gene signatures and longer timepoints.

In summary, we systematically unveiled the deregulation of biological processes and pathways that resulted from MI in heart, liver, muscle, and adipose tissue by integrating transcriptomic data and the use of biological networks. We also identified the key clusters and central genes using generated tissue-specific CNs. In this study, we demonstrated a strategy to utilize multi-tissue transcriptomic data to identify alteration of biological processes and pathways to systemically explore the effect of a disease.

Author Contribution

MK performed the animal experiments, MA performed the computational analysis and analyzed the clinical data together with RB, SD, HT, MU, MC, JW, DE, CZ, AM, and JB

404 coordinated the generation of the clinical data. MA, MK, AM and JB wrote the paper and all
405 authors were involved in editing the paper.
406
407 **Acknowledgements**
408 This work was financially supported by the Knut and Alice Wallenberg Foundation, Swedish
409 Research Foundation and Swedish Heart-Lung Foundation.
410
411 **Conflict of Interest**
412 JW, MC, DE are employees at AstraZeneca. The other authors declare no conflict of interest.
413

Material and Methods

Induction of MI

10-week-old male C57Bl/6N mice were fasted for 4 h before induction of myocardial infarction. The mice were then anesthetized with isoflurane, orally intubated, and connected to a small-animal ventilator (SAR-830, Geneq, Montreal, Canada) distributing a mixture of oxygen, air and 2–3% isoflurane. ECG electrodes were placed on the extremities, and cardiac rhythm was monitored during surgery. An incision was made between the 4th and 5th ribs to reveal the upper part of the anterior left ventricle (LV) wall and the lower part of the left atrium. Myocardial infarction was induced by ligating the left anterior descending (LAD) coronary artery immediately after the bifurcation of the left coronary artery 1. The efficacy of the procedure was immediately verified by characteristic ECG changes, and akinesis of the LV anterior wall. After verification of the infarction, the lungs were hyperinflated, positive end-expiratory pressure was applied, and the chest was closed. Sham mice were handled identically, but no ligation of the LAD coronary artery was performed (and thus, no ischemia was induced in these mice). The mice received an intraperitoneal injection of 0.1 ml buprenorphine to relieve postoperative pain and were allowed to recover spontaneously after stopping isoflurane administration. Mice were killed with an overdose of isoflurane 6 h or 24 h after occlusion or sham operation. We collected the left ventricle (the whole left ventricle containing mainly infarcted tissue) of the heart, whereas white adipose tissue (WAT) was collected from the abdomen and musculus soleus was taken as the muscle tissue. Mouse hearts and biopsies from the liver, muscle and WAT were snap-frozen in liquid nitrogen and stored at -80°C until analysis. All mice studies were approved by the local animal ethics committee and conform to the guidelines from Directive 2010/63/EU of the European Parliament on the protection of animals used for scientific purposes.

Echocardiography in mice

Echocardiographic examination, using VisualSonics VEVO 2100 system (VisualSonics Inc, Ontario, Canada), which includes an integrated rail system for consistent positioning of the ultrasound probe was performed 6 and 24 h after an MI to determine the size of the MI. We calculated infarct size based on wall motion score index (WMSI) 24 h after myocardial infarction by a 16-segments model on 3 short axis images, as 0 for normal, ½ for reduced wall thickening and excursion in a segment and 1 for no wall thickening and excursion in a segment. WMSI was calculated as the sum of scores divided by the total number of segments. Hair

447 removal gel was applied to isofluorane-anesthetized (1.2%) mice chest to minimize resistance
448 to ultrasonic beam transmission. The mice were then placed on a heating pad and extremities
449 were connected to an ECG. A 55 MHz linear transducer (MS550D) was used for imaging. An
450 optimal parasternal long axis (LAX) cine loop of >1000 frames/s was acquired using the ECG-
451 gated kilohertz visualization technique. Parasternal short axis cine-loops were acquired at 1, 3,
452 and 5 mm below the mitral annulus. Infarct size was calculated based on wall motion score
453 index 6 and 24 hours after myocardial infarction by a 16-segments model on LAX and 3 short
454 axis images view, as 0 for normal, ½ for reduced wall thickening and excursion in a segment
455 and 1 for no wall thickening and excursion in a segment. The data were evaluated using
456 VevoStrain™ software system (VisualSonics Inc, Ontario, Canada).
457
458 ***RNA extraction and sequencing***
459 Total RNA was isolated from homogenized heart tissue using RNeasy Fibrous Tissue Mini Kit
460 (Qiagen). cDNA was synthesized with the high-capacity cDNA Reverse Transcription Kit
461 (Applied Biosystems) and random primers. mRNA expression of genes of interest was analyzed
462 with TaqMan real-time PCR in a ViiA™ 7 system (Applied Biosystems). RNA sequencing
463 library were prepared with Illumina RNA-Seq with Poly-A selections. Subsequently, the
464 libraries were sequenced on NovaSeq6000 (NovaSeq Control Software 1.6.0/RNA v3.4.4) with
465 a 2x51 setup using 'NovaSeqXp' workflow in 'S1' mode flow cell. The Bcl was converted to
466 FastQ by bcl2fastq_v2.19.1.403 from CASAVA software suite (Sanger/phred33/Illumina 1.8+
467 quality scale).
468
469 ***RNA-sequencing data analysis***
470 The raw RNA-sequencing results were processed using Kallisto [46] with index file generated
471 from the Ensembl mouse reference genome (Release-96) [47]. The output from Kallisto, both
472 estimated count and TPM (Trancript per kilobase million), were subsequently mapped to gene
473 using the mapping file retrieved from Ensembl BioMart website, by filtering only protein
474 coding genes and transcripts. Genes with mean expression less than 1 TPM in each condition
475 were filtered. For data exploration, we used PCA from sklearn package [48] in Python 3.7 and
476 used TPM values as the input.
477 Subsequently, we performed differential gene expression analysis using DESeq2 package in
478 R. We utilized the capabilities from DESeq2 to normalize the rounded estimated count data
479 and to correct for confounding factors (such as time). To define a gene as differentially

480 expressed (DEGs), a gene has to fulfill a criterion of FDR < 5%. The results of differential
481 expression analysis were then used for functional analysis.
482
483 We checked the tissue specificity of the DEGs in each tissue with the data from Mouse Gene
484 Atlas [25]. For all the tissue-specific genes, we also checked their human-homolog genes in the
485 human secretome database [49].
486
487 ***Functional analysis***
488 We performed functional analysis using the R package PIANO [50]. As the input, we used the
489 fold changes and p-values from the DESeq2, and also GO BP and KEGG pathways gene-set
490 collections from Enrichr [22,23], and metabolites from Mouse Metabolic Reaction database [18].
491 To define a process or pathway as significant, we used a cut off of FDR < 5% for the distinct
492 direction of PIANO (both up and down).
493
494 ***Co-expression network generation***
495 We generated the co-expression network by generating gene-gene Spearman correlation ranks
496 within a tissue type, using *spearmanr* function from SciPy [51] in Python 3.7. Using the same
497 environment, we performed multiple hypothesis testing using Benjamini-Hochberg method
498 from *statsmodels* [52]. Correlation data were filtered with criterion of adjusted p-value < 5%.
499
500 The top 5% of filtered correlation results were then loaded into iGraph module [53] in Python
501 3.7 as an unweighted network. To find the subnetworks, we employed the Leiden clustering
502 algorithm [21] with *ModularityVertexPartition* method. Each cluster was analyzed by using
503 Enrichr [22,23] to get the enriched GO BP and KEGG pathways. Criterion FDR < 0.05 were used
504 to find the significantly enriched terms. Clusters with less than 30 genes were discarded, to be
505 able to get significant functional analysis results. Since GO BP was relatively sparse, we used
506 Revigo [24] to summarize the GO BP into a higher level. Revigo was further employed to build
507 a GO BP network. Clustering coefficient was calculated based on the average local clustering
508 coefficient function within iGraph.
509

Multi-tissue metabolic modeling

We combined tissue-specific models (of heart, liver, muscle, adipose and small intestine) constructed previously [18] in a multi-tissue model by adding an additional compartment representing the plasma, which allows the exchange of metabolites among different tissues. Blocked reactions that could not carry fluxes (and the unused metabolites and genes linked to these reactions) were removed from the models. In addition, the dietary input reactions and constraints were added to the small intestine model to simulate the food intake (**Table S7**). Specifically, we assumed that the mice weighed 30 g and consumed 4.5 g chow diet per day (15 g/100 g body weight) based on a previous study [54]. We also calculated the tissue-specific resting energy expenditures and set them as mandatory metabolic constraints based on previous studies and resting energy expenditure for other tissues was incorporated by including a mandatory glucose secretion flux out from the system with the lower bound calculated based on ATP (**Table S7**) [54].

To simulate the metabolic flux distribution in the sham-operated mice, we set the lipid droplet accumulation reaction in adipose tissue (m3_Adipose_LD_pool) as the objective function so that the energy additional to the resting energy expenditure will be stored as fat; we used parsimonious FBA to calculate the flux distribution. To simulate the flux distribution after an MI, we used the previously developed method Relative Metabolic Difference ver. 2 (RMetD2) [55] to integrate transcriptomic data. In brief, RMetD2 calculates the expected fluxes of reactions based on their reference fluxes and fold changes of gene expression, and searches for a flux distribution that is close to the expected fluxes while subject to the model constraints.

Validation of the results

We validated our findings by performing similar steps of RNA sequencing and functional analysis for the publicly available mouse MI datasets GSE104187 and GSE52313 [14,15].

Data and code availability

All raw RNA-sequencing data generated from this study can be accessed through accession number GSE153485. Codes used during the analysis are available on https://github.com/sysmedicine/ArifEtAll_2020_MultiTissueMI

References

1 WHO. *Cardiovascular diseases (CVDs) Fact sheets*, <https://www.who.int/news-room/fact-sheets/detail/cardiovascular-diseases-(cvds)> (2019).

2 Mardinoglu, A., Boren, J., Smith, U., Uhlen, M. & Nielsen, J. The employment of systems biology in gastroenterology and hepatology. *Nat. Rev. Gastroenterol. Hepatol* (2017).

3 Mardinoglu, A. & Nielsen, J. New paradigms for metabolic modeling of human cells. *Current Opinion in Biotechnology* **34**, 91-97 (2015).

4 Nielsen, J. Systems biology of metabolism: a driver for developing personalized and precision medicine. *Cell metabolism* **25**, 572-579 (2017).

5 Turanli, B. *et al.* Discovery of therapeutic agents for prostate cancer using genome-scale metabolic modeling and drug repositioning. *EBioMedicine* **42**, 386-396 (2019).

6 Benfeitas, R. *et al.* Characterization of heterogeneous redox responses in hepatocellular carcinoma patients using network analysis. *EBioMedicine* **40**, 471-487 (2019).

7 Bidkhori, G. *et al.* Metabolic network-based stratification of hepatocellular carcinoma reveals three distinct tumor subtypes. *Proceedings of the National Academy of Sciences* **115**, E11874-E11883 (2018).

8 Lee, S. *et al.* Integrated network analysis reveals an association between plasma mannose levels and insulin resistance. *Cell metabolism* **24**, 172-184 (2016).

9 Lee, S. *et al.* Network analyses identify liver-specific targets for treating liver diseases. *Molecular systems biology* **13** (2017).

10 Bakhtiarizadeh, M. R., Hosseinpour, B., Shahhoseini, M., Korte, A. & Gifani, P. Weighted Gene Co-expression Network Analysis of Endometriosis and Identification of Functional Modules Associated With Its Main Hallmarks. *Frontiers in Genetics* **9**, doi:10.3389/fgene.2018.00453 (2018).

11 Mukund, K. & Subramaniam, S. Co-expression network approach reveals functional similarities among diseases affecting human skeletal muscle. *Frontiers in physiology* **8**, 980 (2017).

12 Pedrotty, D. M., Morley, M. P. & Cappola, T. P. Transcriptomic biomarkers of cardiovascular disease. *Progress in cardiovascular diseases* **55**, 64-69 (2012).

13 Das, S. *et al.* Transcriptomics of cardiac biopsies reveals differences in patients with or without diagnostic parameters for heart failure with preserved ejection fraction. *Scientific reports* **9**, 3179 (2019).

14 Ounzain, S. *et al.* Genome-wide profiling of the cardiac transcriptome after myocardial infarction identifies novel heart-specific long non-coding RNAs. *European heart journal* **36**, 353-368 (2014).

15 Williams, A. L. *et al.* HIF1 mediates a switch in pyruvate kinase isoforms after myocardial infarction. *Physiological genomics* **50**, 479-494 (2018).

16 Priest, C. & Tontonoz, P. Inter-organ cross-talk in metabolic syndrome. *Nature Metabolism*, doi:10.1038/s42255-019-0145-5 (2019).

17 Lex, A., Gehlenborg, N., Strobelt, H., Vuillemot, R. & Pfister, H. UpSet: visualization of intersecting sets. *IEEE transactions on visualization and computer graphics* **20**, 1983-1992 (2014).

18 Mardinoglu, A. *et al.* The gut microbiota modulates host amino acid and glutathione metabolism in mice. *Molecular Systems Biology* **11**, 834, doi:10.15252/msb.20156487 (2015).

19 Lima, I., Peres, W., Cruz, S. & Ramalho, A. Association of Ischemic Cardiovascular Disease with Inadequacy of Liver Store of Retinol in Elderly Individuals. *Oxidative medicine and cellular longevity* **2018** (2018).

20 Palace, V. P., Hill, M. F., Khaper, N. & Singal, P. K. Metabolism of vitamin A in the heart increases after a myocardial infarction. *Free Radical Biology and Medicine* **26**, 1501-1507 (1999).

21 Traag, V. A., Waltman, L. & van Eck, N. J. From Louvain to Leiden: guaranteeing well-connected communities. *Scientific reports* **9** (2019).

22 Chen, E. Y. *et al.* Enrichr: interactive and collaborative HTML5 gene list enrichment analysis tool. *BMC Bioinformatics* **14**, 128, doi:10.1186/1471-2105-14-128 (2013).

23 Kuleshov, M. V. *et al.* Enrichr: a comprehensive gene set enrichment analysis web server 2016 update. *Nucleic Acids Research* **44**, W90-W97, doi:10.1093/nar/gkw377 (2016).

24 Supek, F., Bošnjak, M., Škunca, N. & Šmuc, T. REVIGO summarizes and visualizes long lists of gene ontology terms. *PloS one* **6**, e21800 (2011).

25 Su, A. I. *et al.* A gene atlas of the mouse and human protein-encoding transcriptomes. *Proceedings of the National Academy of Sciences of the United States of America* **101**, 6062-6067, doi:10.1073/pnas.0400782101 (2004).

26 Kiyuna, L. A., e Albuquerque, R. P., Chen, C.-H., Mochly-Rosen, D. & Ferreira, J. C. B. Targeting mitochondrial dysfunction and oxidative stress in heart failure: challenges and opportunities. *Free Radical Biology and Medicine* **129**, 155-168 (2018).

27 Palaniyandi, S. S., Qi, X., Yogalingam, G., Ferreira, J. C. B. & Mochly-Rosen, D. Regulation of mitochondrial processes: a target for heart failure. *Drug Discovery Today: Disease Mechanisms* **7**, e95-e102 (2010).

28 Camara, A. K., Zhou, Y., Wen, P.-C., Tajkhorshid, E. & Kwok, W.-M. Mitochondrial VDAC1: a key gatekeeper as potential therapeutic target. *Frontiers in physiology* **8**, 460 (2017).

29 Schwertz, H. *et al.* Myocardial ischemia/reperfusion causes VDAC phosphorylation which is reduced by cardioprotection with a p38 MAP kinase inhibitor. *PROTEOMICS* **7**, 4579-4588, doi:10.1002/pmic.200700734 (2007).

30 Yada, T. *et al.* Cardioprotective role of endogenous hydrogen peroxide during ischemia-reperfusion injury in canine coronary microcirculation in vivo. *American Journal of Physiology-Heart and Circulatory Physiology* **291**, H1138-H1146 (2006).

31 Sun, W. *et al.* Cardiac-specific deletion of the Pdha1 gene sensitizes heart to toxicological actions of ischemic stress. *Toxicological Sciences* **151**, 193-203 (2016).

32 Mardinoglu, A. *et al.* Personal model-assisted identification of NAD+ and glutathione metabolism as intervention target in NAFLD. *Molecular systems biology* **13** (2017).

33 Alexander, M. *et al.* Non-alcoholic fatty liver disease and risk of incident acute myocardial infarction and stroke: findings from matched cohort study of 18 million European adults. *bmj* **367**, l5367 (2019).

34 Tran, D. H. & Wang, Z. V. Glucose Metabolism in Cardiac Hypertrophy and Heart Failure. *Journal of the American Heart Association* **8**, e012673 (2019).

35 Miyamoto, T., Katayama, Y. & Harano, Y. Blood ketone body as a stress marker in acute myocardial infarction. *Nihon Kyukyu Igakukai Zasshi* **10**, 621-622 (1999).

36 Zhou, Y. *et al.* Loss of Filamin C Is Catastrophic for Heart Function. *Circulation* **141**, 869-871 (2020).

37 Hall, C. L. *et al.* RNA sequencing-based transcriptome profiling of cardiac tissue implicates novel putative disease mechanisms in FLNC-associated arrhythmogenic cardiomyopathy. *International journal of cardiology* **302**, 124-130 (2020).

38 Diviani, D., Dodge-Kafka, K. L., Li, J. & Kapiloff, M. S. A-kinase anchoring proteins: scaffolding proteins in the heart. *American Journal of Physiology-Heart and Circulatory Physiology* **301**, H1742-H1753 (2011).

39 Turnham, R. E. & Scott, J. D. Protein kinase A catalytic subunit isoform PRKACA; History, function and physiology. *Gene* **577**, 101-108 (2016).

40 Bers, D. M. Calcium cycling and signaling in cardiac myocytes. *Annu. Rev. Physiol.* **70**, 23-49 (2008).

41 Zhong, X., Qian, X., Chen, G. & Song, X. The role of galectin-3 in heart failure and cardiovascular disease. *Clinical and Experimental Pharmacology and Physiology* **46**, 197-203 (2019).

42 Suthahar, N. *et al.* Galectin-3 activation and inhibition in heart failure and cardiovascular disease: an update. *Theranostics* **8**, 593 (2018).

43 Ren, J., Pulakat, L., Whaley-Connell, A. & Sowers, J. R. Mitochondrial biogenesis in the metabolic syndrome and cardiovascular disease. *Journal of molecular medicine* **88**, 993-1001 (2010).

44 Siasos, G. *et al.* Mitochondria and cardiovascular diseases—from pathophysiology to treatment. *Annals of translational medicine* **6** (2018).

45 Piantadosi, C. A. & Suliman, H. B. Transcriptional control of mitochondrial biogenesis and its interface with inflammatory processes. *Biochimica et Biophysica Acta (BBA)-General Subjects* **1820**, 532-541 (2012).

46 Bray, N. L., Pimentel, H., Melsted, P. & Pachter, L. Near-optimal probabilistic RNA-seq quantification. *Nature biotechnology* **34**, 525 (2016).

47 Zerbino, D. R. *et al.* Ensembl 2018. *Nucleic Acids Research* **46**, D754-D761, doi:10.1093/nar/gkx1098 (2017).

48 Pedregosa, F. *et al.* Scikit-learn: Machine learning in Python. *Journal of machine learning research* **12**, 2825-2830 (2011).

49 Uhlén, M. *et al.* The human secretome. *Science Signaling* **12**, eaaz0274, doi:10.1126/scisignal.aaz0274 (2019).

50 Väremo, L., Nielsen, J. & Nookaew, I. Enriching the gene set analysis of genome-wide data by incorporating directionality of gene expression and combining statistical

hypotheses and methods. *Nucleic Acids Research* **41**, 4378-4391, doi:10.1093/nar/gkt111 (2013).

51 Jones, E., Oliphant, T. & Peterson, P. SciPy: Open source scientific tools for Python. (2001).

52 Perktold, J., Seabold, S. & Taylor, J. (Oct, 2017).

53 Csardi, G. & Nepusz, T. The igraph software package for complex network research. *InterJournal, Complex Systems* **1695**, 1-9, doi:10.5281/zenodo.3630268 (2006).

54 Kummitha, C. M., Kalhan, S. C., Saidel, G. M. & Lai, N. Relating tissue/organ energy expenditure to metabolic fluxes in mouse and human: experimental data integrated with mathematical modeling. *Physiological reports* **2** (2014).

55 Zhang, C. *et al.* RMetD2: a tool for integration of relative transcriptomics data into Genome-scale metabolic models. *BioRxiv*, 663096 (2019).

Table

Table 1 Properties of the co-expression network

Tissue	# of Genes	# of Edges	# of Clusters	Modularity Scores
Heart	8793	1570898	7	0.540179085
Liver	7760	1103589	6	0.577273459
Muscle	8834	1660603	7	0.521239124
Adipose	10790	2636378	8	0.495469439

Supplementary Tables

Table S1 Differential Expression Analysis Results

Table S2 KEGG Pathways

Table S3 Gene Ontology Biological Processes

Table S4 DEG comparison between Liver and other tissues

Table S5 Reporter Metabolite Analysis

Table S6 Enrichment Analyses of Clusters, Clusters properties

Table S7 Food Intake, Energy Expenditure, and Flux Balance Analysis (FBA) of Whole-Body Modeling

Table S8 Validation Result (Differential Expression and Functional Analysis)

Table S9 Detailed Information of 16 Key Genes that are DEGs in at least 3 tissues and Neighbors and Functional Analysis Results of The Neighbors of 4 key genes

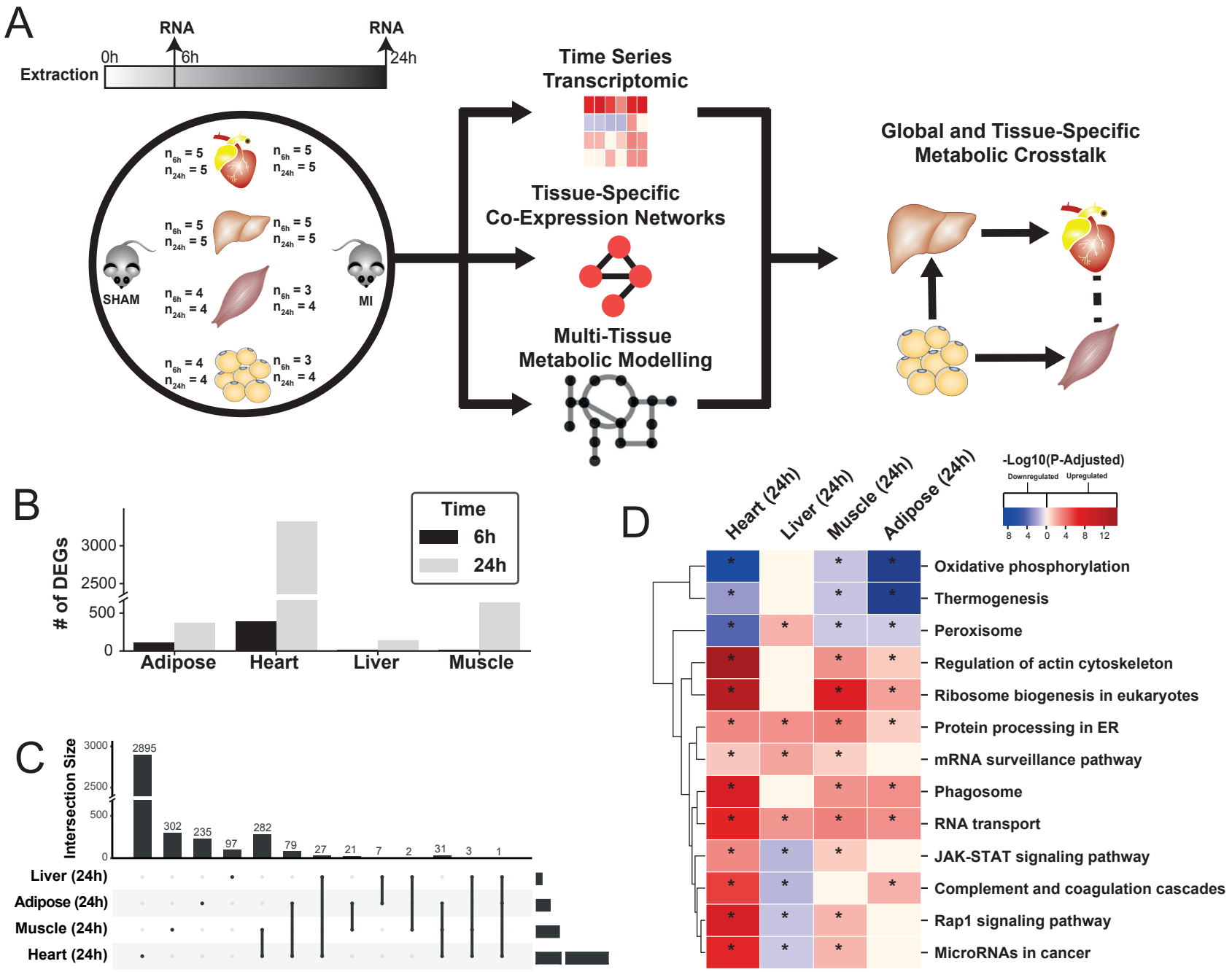

Figure 1 (A) Overview of this study (B) Number of differentially expressed genes for each tissue at each time point. Effect of MI shown to be more pronounced after 24 h. (C) UpSet plot to show intersection between differentially expressed genes (FDR < 5%) in different tissues. The plot showed that each tissue has its specific set of genes that were affected by MI. (D) KEGG pathway analysis (FDR < 0.05 in at least 3 tissues) for 24 hours post MI compared to its control for each tissue. We observed that 141 (5 upregulated) and 125 (14 upregulated) pathways are significantly altered in heart 6 and 24 h after infarction, respectively. For other tissues, we found that 24 (9 upregulated), 61 (54 upregulated) and 48 (15 upregulated) pathways are altered in liver, muscle, and adipose, respectively.

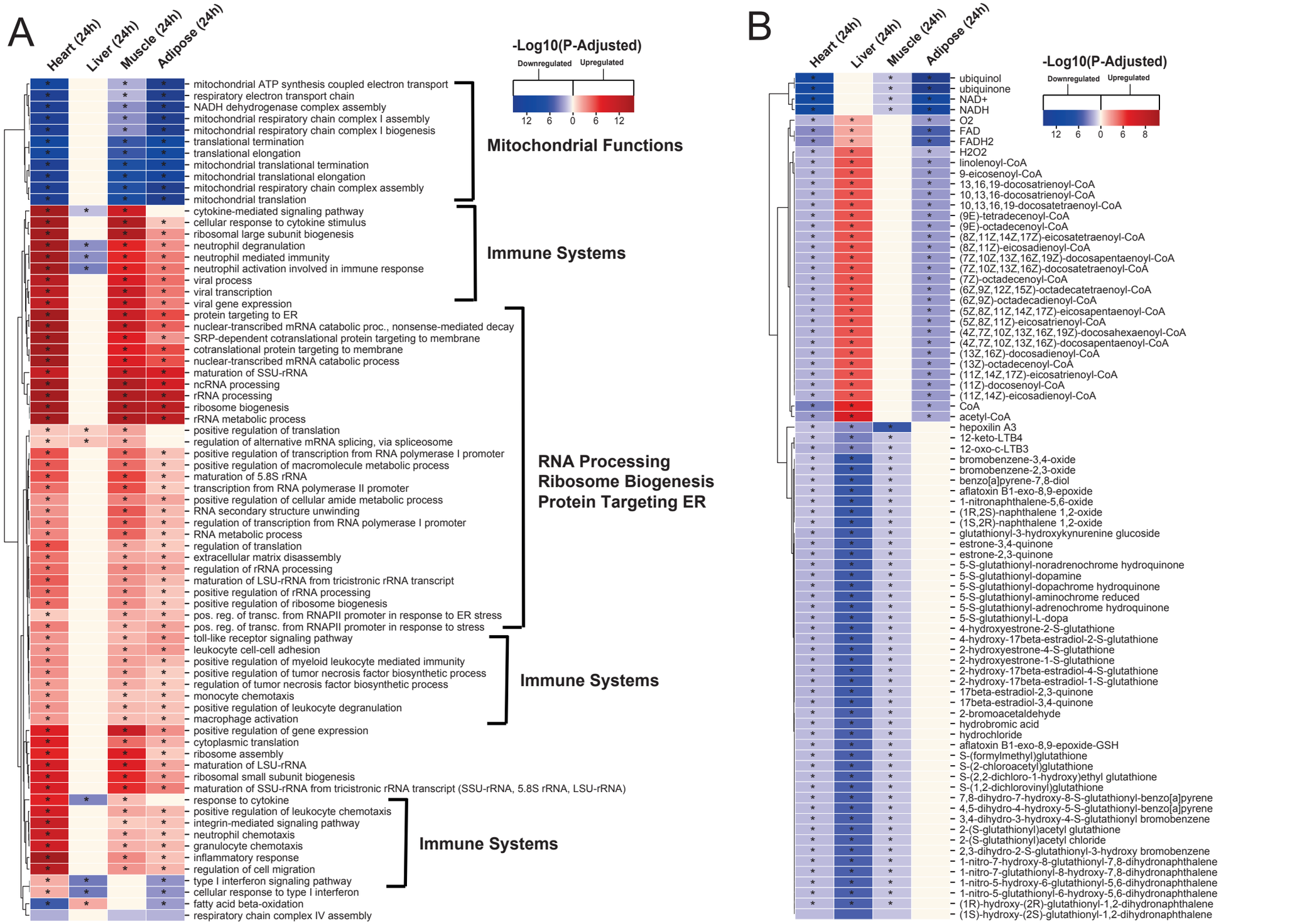

Figure 2 (A) Functional analysis with GO (FDR < 0.05% in at least 3 tissues) revealed that 944 (919 upregulated) and 1019 (970 upregulation) BPs are significantly altered in heart 6 and 24 h after infarction, respectively. The results also showed 38 (16 upregulated), 376 (357 upregulated) and 193 (116 upregulated) BPs are significantly altered 24 h after infarction in liver, muscle and adipose, respectively. Most tissues show significant alterations in multiple biological processes, including mitochondrial functions, RNA processes, cell adhesion, ribosome and immune systems. The results of this analysis showed alterations concordant with those observed for KEGG pathways. (B) Reporter metabolites analysis shows significant alternation in important metabolites. Our analysis revealed that 169, 324, 118 and 51 reporter metabolites are significantly altered in heart, liver, skeletal muscle and adipose tissues, respectively, at 24 h post-infarction (Table S4)

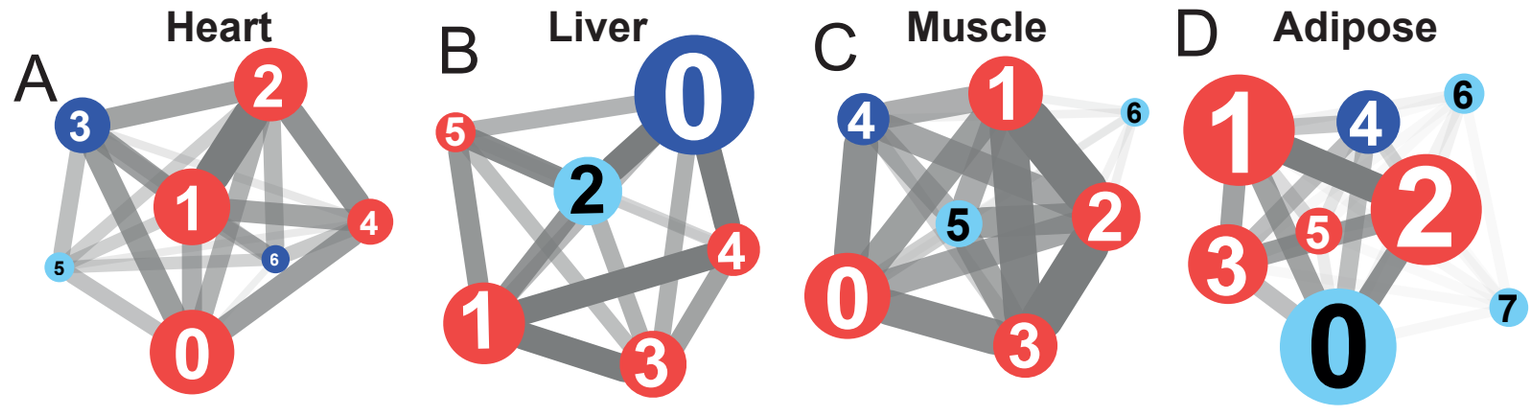

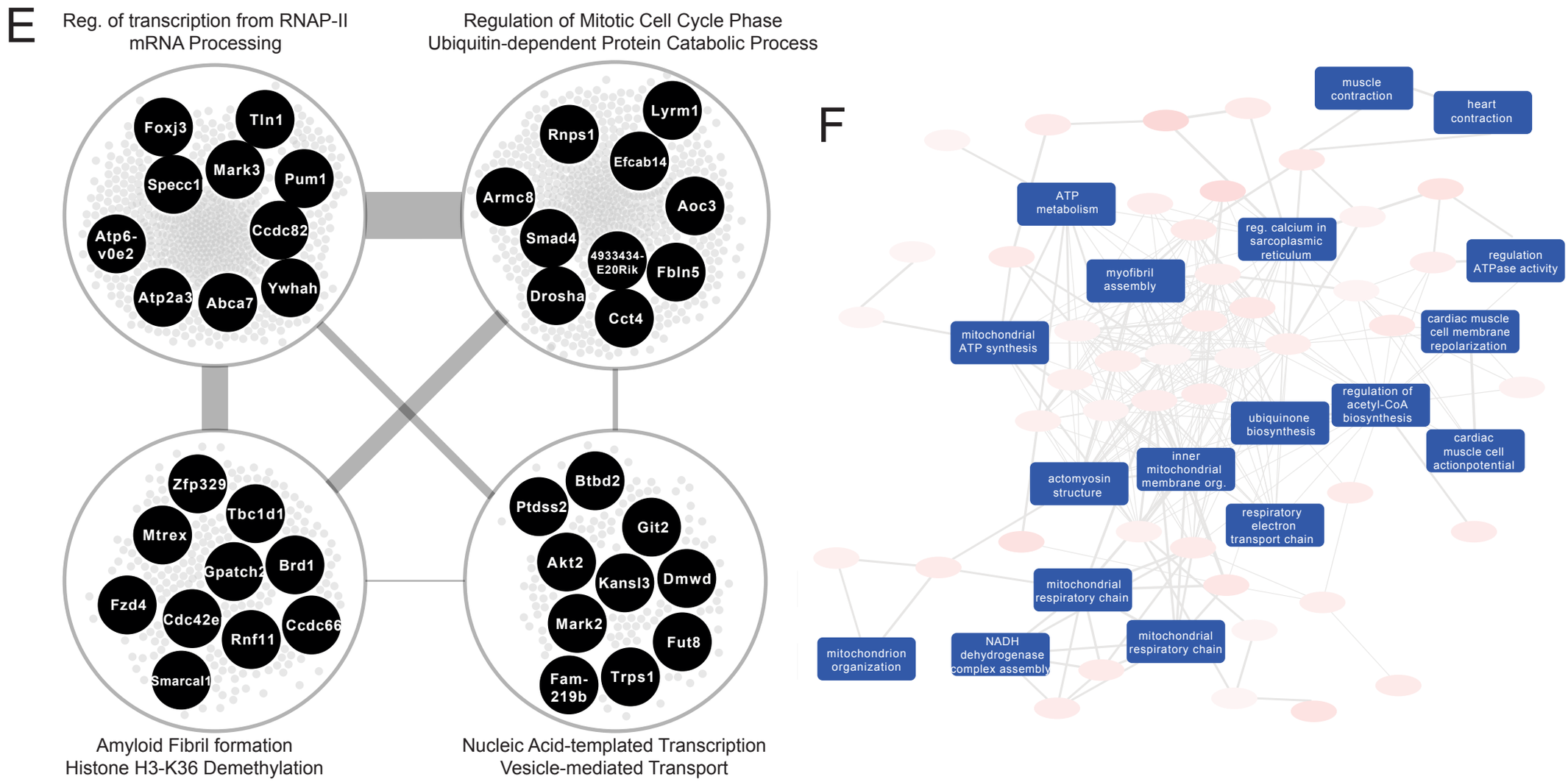

Figure 3 Network analyses. (A) Heart co-expression network clusters with superimposed DEGs 24 h post-infarction (Blue = down-regulated, Red = up-regulated) marked with the cluster numbers. The edges between the clusters were aggregation of the inter-cluster edges (B) Liver. (C) Muscle. (D) Adipose. (E) Intersection of the most central clusters in all tissues shows that the central architecture of the network was conserved in all tissues. We found 4 sub-clusters within the network intersection. Top 10 most connected genes are marked in black. (F) Enriched GO BP in heart-specific cluster generated by Revigo.

A

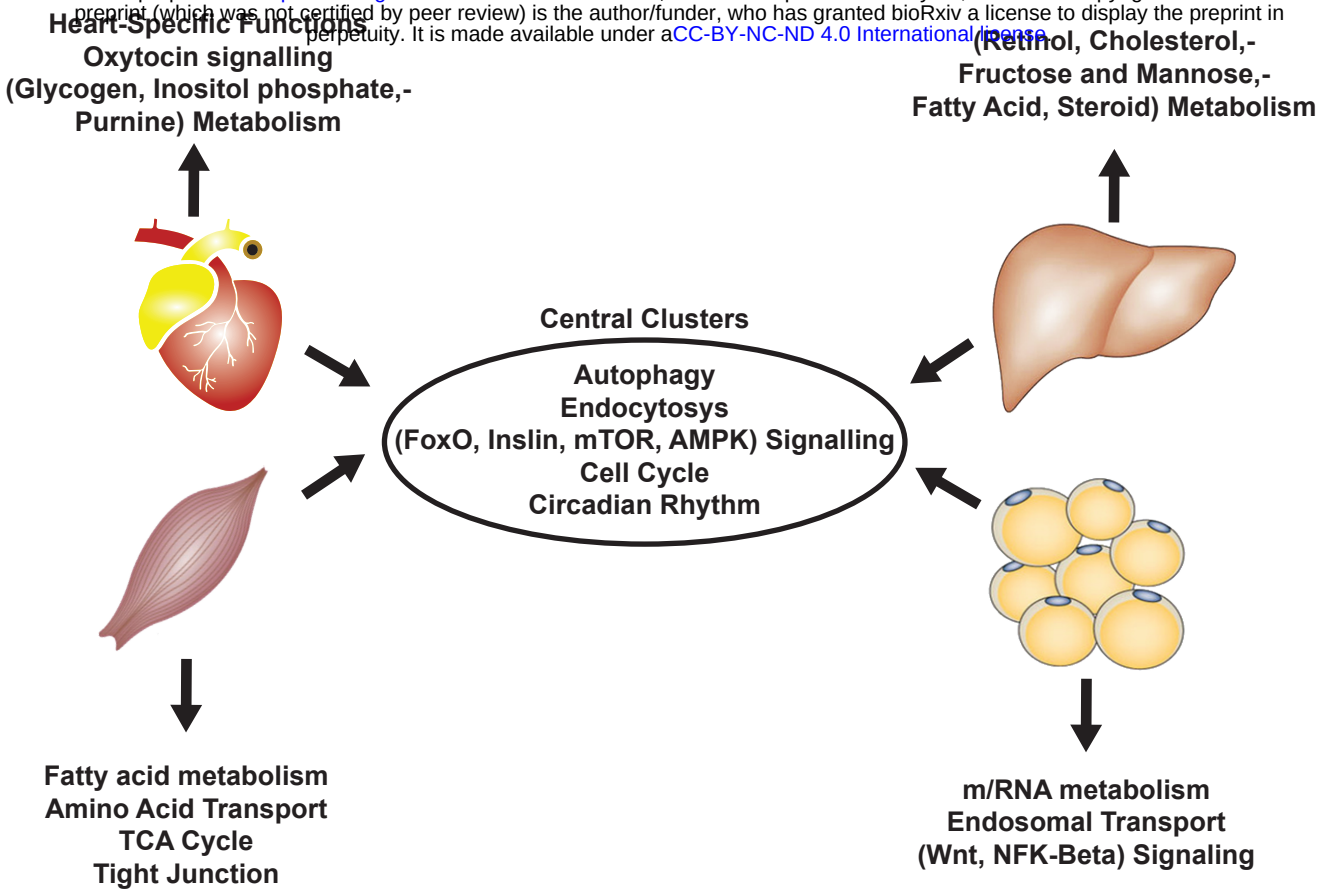

B

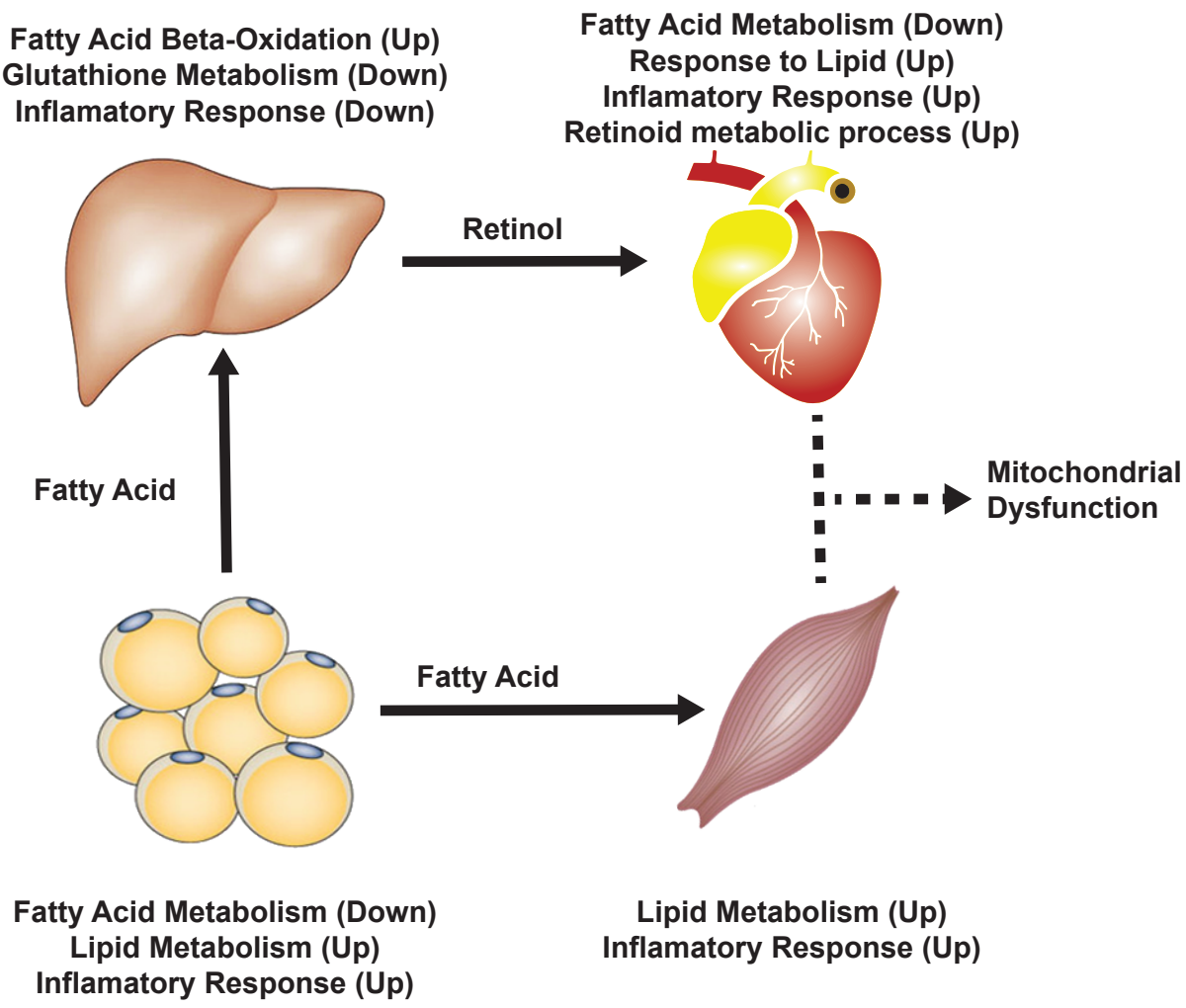

Figure 4 (A) Similarity of functions in the most central cluster and specific functions of each tissue-specific cluster. (B) Functional analysis for each tissue and hypothesized flow of metabolites

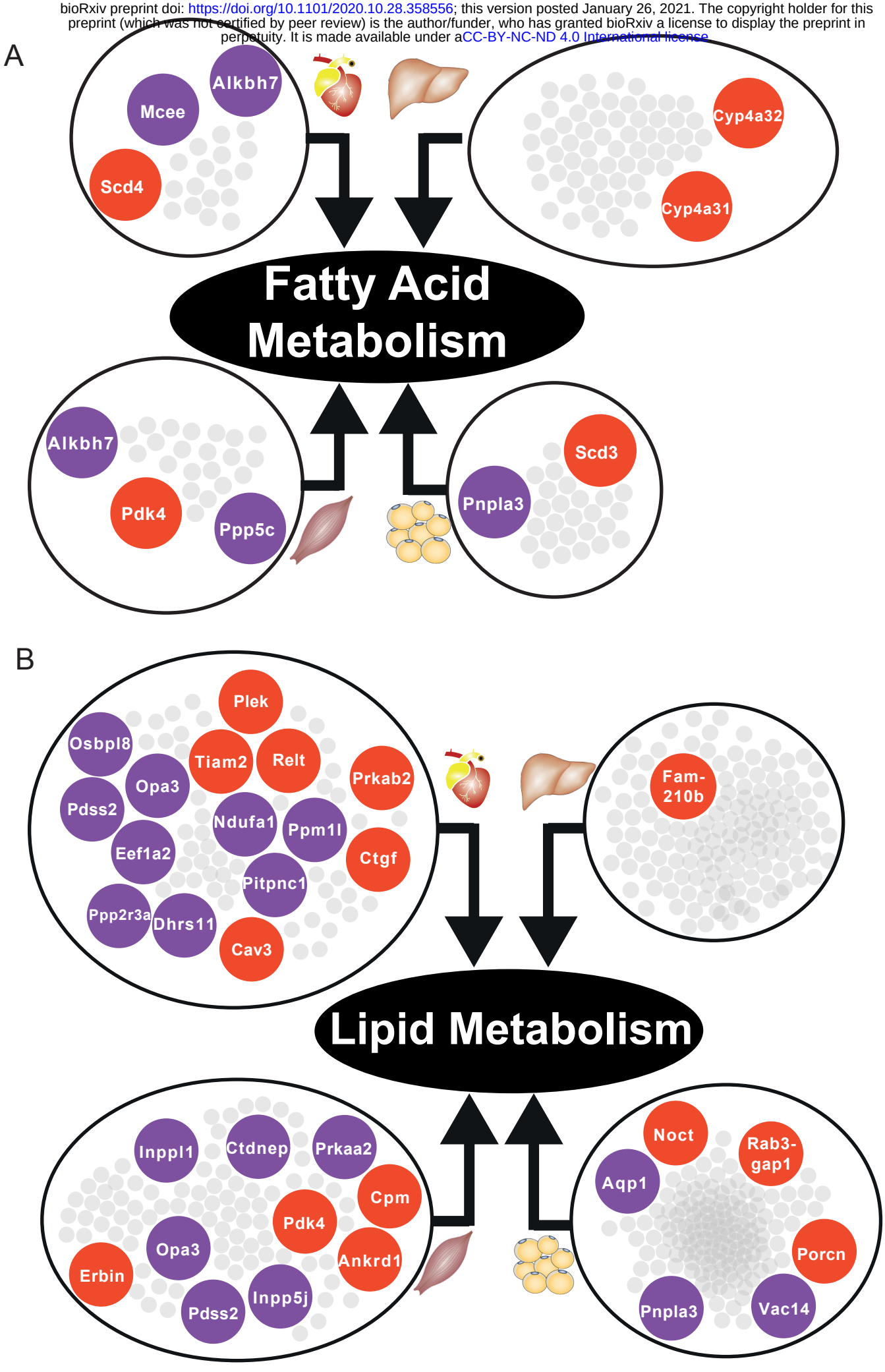

Figure 5 (A) Significantly differentially expressed central genes of each tissue-specific cluster to fatty acid metabolism, as one of the most affected metabolic process. (B) Lipid metabolism. Red = upregulated, blue = downregulated.

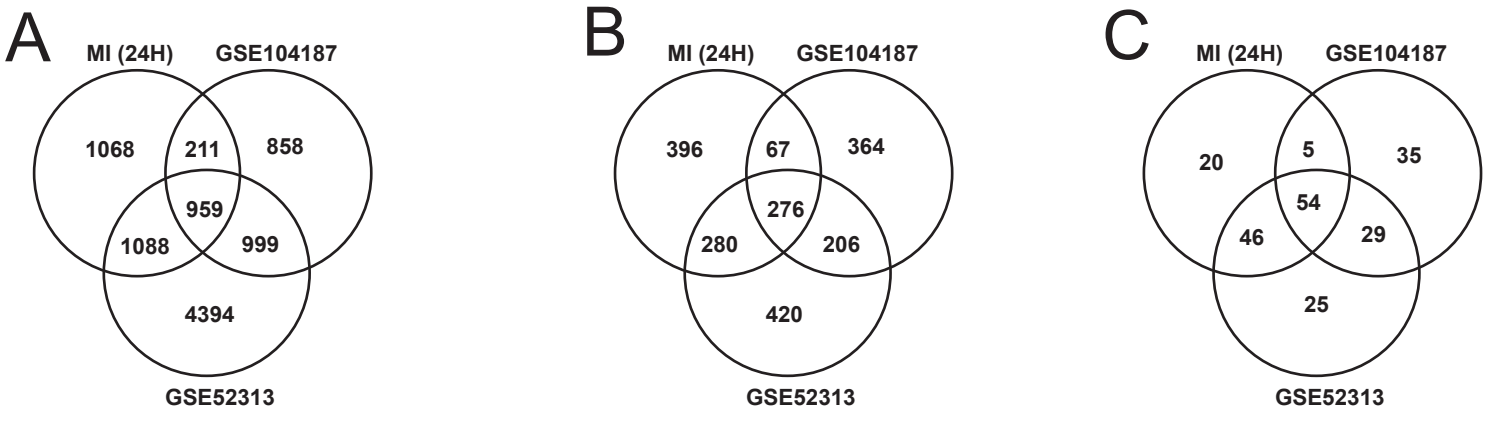

Figure 6 (A) DEGs intersection of our data and validation cohort (B) & (C) Intersection of functional analysis results (GO BP and KEGG Pathways) of our data and validation cohort